1-11-2007

Chemical and dynamical processes in the mesospheric emissive layer. First results of stereoscopic observations

M. Faivre
Clemson University

G. Moreels
Observatoire de Besançon, Besançon, France

Pierre-Dominique Pautet
Utah State University, dominiquepautet@gmail.com

J. Clairemidi
Observatoire de Besançon, Besançon, France

F. Dumont
Observatoire de Besançon, Besançon, France

O. Lorin
Observatoire de Besançon, Besançon, France

Recommended Citation

Faivre M., Moreels G., Pautet P.-D., Clairemidi J., Dumont F., Lorin O., and Colas F., Chemical and dynamical processes in the mesospheric emissive layer. First results of stereoscopic observations, J. Geophys. Res., 112, D013016, 2007

Chemical and dynamical processes in the mesospheric emissive layer: First results of stereoscopic observations

M. Faivre,[1] G. Moreels,[2] D. Pautet,[3] J. Clairemidi,[2] F. Dumont,[2] O. Lorin,[2] and F. Colas[4]

Received 16 February 2005; revised 13 April 2006; accepted 29 August 2006; published 11 January 2007.

[1] The mesospheric emissive layer is an efficient tracer of the dynamical processes propagating in the atmosphere at that level. CCD images in the near infrared taken from the ground at slant angles often reveal the existence of wavy fields. A series of such images has been transformed, using matrix operations, producing a downward satellite-type view that covers a circular area of radius ~1000 km at the altitude of the layer. The Fourier characteristics of the wave system are measured using a Morlet-type wavelet generator function with horizontal wavelengths of mostly ~20–40 km and 100–150 km and temporal periods of ~15–30 min. An oxygen-hydrogen model is used to evaluate the response of the emissive layer to a progressive density wave. The altitude of the layer is modulated with an amplitude of ~0.8–1.8 km when a density wave propagates vertically. The layer thickness is slightly modulated and is equal to ~7 km. Stereoscopic pairs of photographs taken simultaneously on 8–9 September 2000 at the Château-Renard and Pic du Midi observatories are used to obtain surface maps of the emission layer barycenter altitude. A stereocorrelation method suitable for low contrast objects without discrete contours is employed. Preliminary results for areas ~50×50 km^2 are presented. The surface maps of the layer barycenter altitude depict the existence of waves. They show the same wavy structure and compare favorably with the maps showing the emission intensity.

Citation: Faivre, M., G. Moreels, D. Pautet, J. Clairemidi, F. Dumont, O. Lorin, and F. Colas (2007), Chemical and dynamical processes in the mesospheric emissive layer: First results of stereoscopic observations, *J. Geophys. Res.*, *112*, D01306, doi:10.1029/2005JD005891.

1. Introduction

[2] Since its discovery and identification by astronomers [*Slipher*, 1929; *Meinel*, 1950; *Herzberg*, 1951], the emission originating from the mesosphere has been considered from different viewpoints by astronomers and atmospheric physicists. For astronomers, it is considered as an additional sky background that needs to be subtracted from their images [*Glass*, 1999]. The emission intensity is neither constant with time nor uniform over the sky. Consequently, when observing in certain wavelength regions, an important fraction of the observing time must be spent in measuring the background in the neighborhood of the astronomical objects of interest [*Pautet et al.*, 2002]. The sky background spectrum is mainly composed of ro-vibronic bands of the OH* molecule, where each band contains several tens of lines. A medium resolution spectrum of OH in the 0.997 ~ 2.25 μm range, based on observations obtained with the ISAAC (Infrared Spectrometer and Array Camera) installed at the first unit telescope of the ESO-VLT, has been reduced by *Rousselot et al.* [2000]. In this spectrum, the wavelength scale is calibrated and the atmospheric lines are identified. As a result, it may be used to determine the wavelengths of the weak lines from distant objects and to avoid possible misidentification of lines in a stellar or galactic spectrum. For atmospheric physicists, the mesospheric emission is an important tracer of the various mechanisms that interact to produce the local steady state in this region.

[3] In this paper, an analysis of the mechanisms that govern the intensity variations of the mesospheric near-IR emission throughout the night will be presented. It will be shown that stereoscopic observations of the emissive layer can give an insight into the chemical and dynamical processes prevailing in this atmospheric region. Hydroxyl emission, a major contributor to the sky background in the near-IR starting at ~700 nm is produced by the reaction between atomic hydrogen and ozone [*Bates and Nicolet*, 1950]

$$H + O_3 \rightarrow OH^* + O_2 \quad (1)$$

[4] The OH* molecule is produced in the fundamental $^2\prod_i$ electronic state. The superscript 2 means that the state is a doublet, each component being inverted as indicated by the subscript *i*. The molecule may be excited to vibrational levels as high as $v = 9$. A small amount of energy is due to the rotation of the molecule around an axis perpendicular to the internuclear line. An emissive transition between two

[1] Astronomy and Physics Department, Clemson University, Clemson, South Carolina, USA.
[2] Observatoire de Besançon, Besançon, France.
[3] Center for Atmospheric and Space Science and Physics Department, Utah State University, Logan, Utah, USA.
[4] Institut de Mécanique Céleste, Observatoire de Paris, Paris, France.

0148-0227/07/2005JD005891

Table 1. List of the Different Sites Where Observations of the Mesospheric Emissive Layer Were Conducted

Observation Site	Coordinates	Altitude	Dates of Observation
Pic de Château-Renard	6°54′E, 44°41′N	2989 m	Jul 1999, 2000, 2001, and 2002 and Sep 2000 and 2001
Observatoire du Pic du Midi	0°09′E, 42°56′N	2861 m	7–11 Sep 2000
Crêt Monniot	6°24′E, 47°01′N	1142 m	18–19 May 1998 and 7–8 Jun 2003
Mont d'Or	6°21′E, 46°43′N	1461 m	7–8 Jun 2003
Observatoire de Haute Provence	5°43′E, 43°56′N	665 m	18–20 Oct 1998

vibrational levels produces a band labeled (υ', υ'') which is composed of closely spaced rotational lines.

[5] The excited OH* molecule is created in a relatively thin atmospheric layer between 82 and 92 km, since its density is proportional, in a first approximation, to the density product [H] [O_3]. The ozone density rapidly diminishes with increasing altitude, whereas the hydrogen does not exist in its atomic form at altitudes lower than 50 km during the day and 75 km during the night. During the day, as a result of UV solar radiation, the mesospheric region is quite chemically active. Molecular oxygen, ozone and water vapor are photodissociated. When the Sun sets, chemical models predict that the ozone concentration rapidly increases within 0.3 to 1 hour. During this brief period of time, a twilight flash of the OH Meinel bands in the airglow was measured by OSIRIS on the ODIN spacecraft [*Degenstein et al.*, 2004]. Later on, after this evening twilight period, models that include chemical and diffusive mechanisms, but do not take into account wave and tide processes, predict that both ozone and hydrogen diminish, leading to a diminution of the OH emission throughout the night. This steady decrease predicted by chemical model calculations is contrary to the observations reported by *Moreels et al.* [1977] and by *Degenstein et al.* [2005]. Indeed, this is quite strong evidence that chemical mechanisms are not the only ones that rule the atmospheric steady state and that dynamical processes play a role that is at least as important. These processes include molecular and eddy diffusion, the influence of tides and the propagation of gravity waves. Tides have periods that are a harmonic of 24 hours [*Teitelbaum et al.*, 1989; *Meriwether and Dao*, 1994; *Sivjee and Walterscheid*, 1994; *Reisin and Scheer*, 1996]. Gravity waves also induce fluctuations in the emissions originating in the 80–100 km altitude range and due to O(^{1}S), $O_2(^1\Sigma)$ and OH* [*Battaner and Molina*, 1980; *Hauchecorne et al.*, 1987; *Swenson et al.*, 1995a; *Taylor et al.*, 1997]. Using a model of diurnal variations in the mesospheric oxygen nightglow, *Ward* [1999] demonstrated that vertical advection is the prime process causing these variations. Two major advances in the knowledge of these dynamical processes were achieved (1) when IR sensitive films became available [*Peterson and Kieffaber*, 1973; *Moreels and Hersé*, 1977; *Hersé et al.*, 1980] and (2) when CCD low noise cameras started to be used in astronomy and atmospheric physics [*Taylor et al.*, 1995; *Pautet et al.*, 2001].

[6] In the present paper, a combination of image analysis techniques is applied to recover both the intensity and barycenter altitude surfaces of the mesospheric OH emission layer from observations of the same atmospheric region taken from two ground-based sites. Observations were conducted with two cameras in a "vis à vis" mode at the observatories of Pic du Midi and Château-Renard. In section 2, a brief description of the observational platforms and of the panoramic photographs obtained with the cameras is given. The ground-based measured intensity images are projected into images that would be provided by a satellite-type view. A wavelet transform is employed to produce the spectral characteristics of the wavefield that appears in these projected images. The intensity wavefield is expected to imply an accompanying structure of the height surface of the emission layer. In section 3, a quantitative analysis of the OH emissive rate, using a photochemical model, is applied to calculate the OH* profile for three different values of the quenching reaction rate. This analysis shows the variation sensitivity of the layer height resulting from a propagating ascending density wave of physically reasonable characteristics. The result is a periodic fluctuation of the barycenter altitude of the layer. Section 4 presents the recently initiated program of stereoimagery of the mesospheric emissive layer to determine barycenter altitudes from intensity images of the previously indicated satellite-type views. Some preliminary results of recovered barycenter altitude surfaces are presented with the associated levels of altitude variability compared to those presented in section 3.

2. Instrumentation and Observational Results

2.1. CCD Cameras and Astronomical Platforms

[7] The instrumentation mainly consists of two CCD cameras mounted on alt-azimuthal astronomical platforms. The orientation of the optical axis of each camera is precisely driven by a computer that also controls the camera, receives and stores the images. Each camera contains a 512 × 512 pixel (19 μm × 19 μm) Thomson CCD cooled to −40°C. It is equipped with an electromechanical shutter and a 15.6 mm *f*/1.3 Angénieux lens. An RG 780 filter placed in front of the lens is used to select the following $\Delta\upsilon$ = 4 OH bands: (4, 0), (5, 1), (6, 2), (7, 3) and (8, 4).

[8] The observation program is conducted to fulfill two objectives: (1) to provide a measurement of the near-IR sky background and of its variations as a function of time and of the direction of the line of sight and (2) to provide a spatial description of the radiation from the emissive layer. Observations are made from the various sites listed in Table 1. In this preliminary work, only observations from Château-Renard and Pic du Midi will be used.

2.2. Satellite-Type Images

[9] Many pictures are taken at low elevation angles in order to take advantage of the perspective effect that allows a description of the atmospheric emission at long distances from the observation site. As a consequence of refraction,

Figure 1. Images taken from Pic de Château-Renard (Hautes-Alpes, 2989 m), 10–11 July 2002. (left) Azimuth = 150°, 0100 UT. (middle) Azimuth = 240°, 0011 UT. (right) Azimuth = 270°, 0016 UT. On the lower right, the Mount Viso is apparent.

objects on the celestial sphere appear raised. This circumstance provides an apparent field of view, when imaging the mesospheric emissive layer, that is actually larger than the geometrical FOV of the front-end lens or telescope of the observing instrument. A detailed account of refraction formulae is given by *Smart* [1977] and in *Danjon* [1959]. Sites at higher altitude offer the advantages of reduced refraction, of clearer skies, and of allowing observations at lower elevation angles. In addition to being such a site, the observatory of Château-Renard in the Hautes-Alpes (altitudes of 2989 m), is also devoid of any telecommunication antennae and other source of obstruction.

[10] The near-IR images of Figure 1 taken at Château-Renard are mainly characterized by the presence of organized structures having the form of ruffled bands or ripples. The overall direction of these bands differs from one picture to the other. However, the spacing between bands increases with increasing elevation for all pictures. A set of 24 adjacent fields of view are assembled to obtain the panorama shown in Figure 2 covering a $360° \times 63°$ FOV. Wide arches extending from one azimuth to the opposite one are clearly apparent. The points where the arches converge at the horizon are vanishing points which indicate the overall direction of parallel lines converging at an infinite distance. The panoramic image, and any individual picture, can be transformed into an image taken at high altitude from above the emission layer, thus removing the geometrical perspective effects. This process is summarized below.

[11] As shown in Figure 3, where the camera is depicted as a pinhole instrument, each point B′ of the CCD retina in C′D′ is matched to a small emissive tube arriving at point B across the emissive layer. If the layer thickness is small in comparison with distances AC and AD, the projection performed by the camera, i.e., the CD segment of the emissive layer projected onto the pixel line of the CCD named C′D′, can also be considered in the reverse direction. A geometrically rectified image of the layer can be obtained by reversing the perspective effect present in the CCD image. The geometric deviation due to refraction and the Van Rhijn effect are both corrected. The resulting image would be similar to an image taken by a virtual camera on board a satellite located vertically above the area of interest. The method developed to invert the perspective effect consists of three successive matrix transformations. It is described in detail by *Pautet and Moreels* [2002] and by *Faivre* [2004]. The technique consists in finding the position of the four corners of each pixel in the frame associated with a virtual camera looking downward on the layer assumed to be at an altitude of 87 km. The shape of the pixels of the virtual image plane becomes trapezoidal. Close to the horizon, the pixels do not overlap any longer and the intensity is calculated using a polynomial interpolation [*Haralick and Watson*, 1981]. Each individual square CCD image produces an angular sector having its apex located at the observation site. These sectors may be assembled in order to obtain a geometrically rectified 360° circular view of the emissive layer.

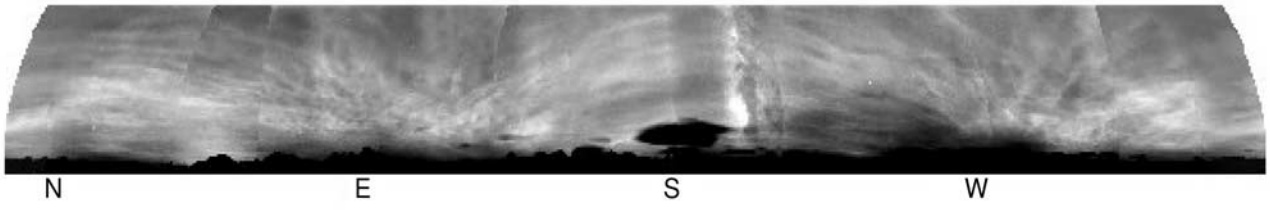

Figure 2. Panorama of 24 consecutive images at Château-Renard from 0017 to 0118 UT on 10–11 July 2002. The wave system is organized in two arches which converge at two vanishing points located at opposite azimuths.

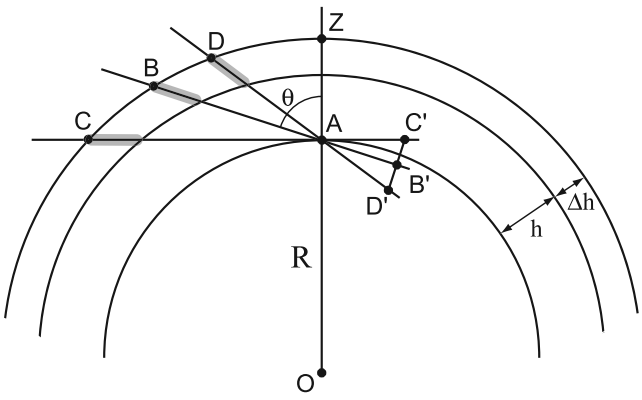

Figure 3. Emissive layer as seen by the CCD camera represented as a pinhole instrument.

[12] Figures 4 and 5 present such a view obtained from Château-Renard (Hautes-Alpes). A contour map of Europe superimposed on the emission shows the extension of the wavefield that is apparent on the photograph. Such two-dimensional views of the OH layer show that the emission is a tracer of atmospheric waves with wavelengths, periods and phase velocities which can be determined.

2.3. Spatial and Temporal Analysis of the Inverted Images

[13] A fast Fourier transform was used by *Faivre et al.* [2003a] to determine the wave parameters from a set of successive photographs taken 3 min apart at Château-Renard, during the night of 11 to 12 July 2002. Typical results from that study consisted of horizontal wavelengths in the range of 25 to 69 km and periods in the range of 10 to 40 min. The calculated mean phase speed was found to be 35 m/s. Using the same set of photographs, a spatial and temporal analysis was conducted, in this study, using a wavelet transform [*Mallat*, 1997]. Compared to a Fourier transform of a time-dependent signal, which gives the frequencies present in the totality of the record, a wavelet transform also provides the evolution with time of the frequency components of the signal. In the present case, the wavelet generator function was of the Morlet type, as given in equation (2):

$$\Psi(\chi) = C\ e^{-\chi^2/2}\ \cos(5\chi) \qquad (2)$$

where C is a normalization constant.

[14] The Morlet wavelet transform is employed to perform separate spatial and temporal analyses of a region of the inverted projected map shown in Figure 6. The observ-

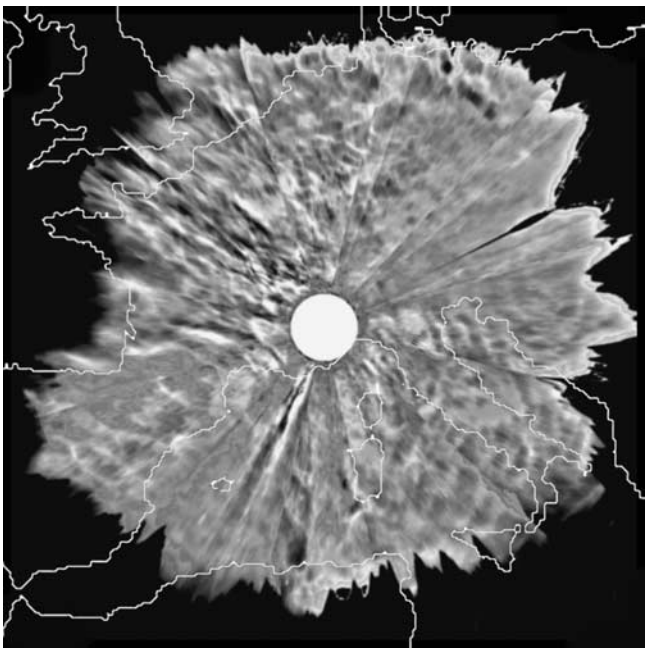

Figure 4. Satellite-type black and white view of the near-IR emissive layer centered on Château-Renard at 0110–0230 UT, 20–21 July 2001. A scaled map of western Europe and North Africa has been superimposed.

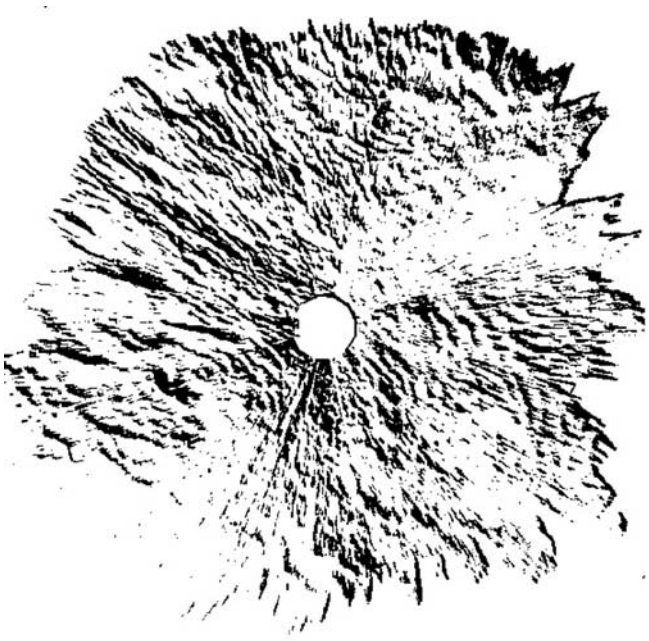

Figure 5. Same view processed with a numerical filter in order to show the wave crests. The Milky Way appears as a diffuse projected radius in the azimuth 24°.

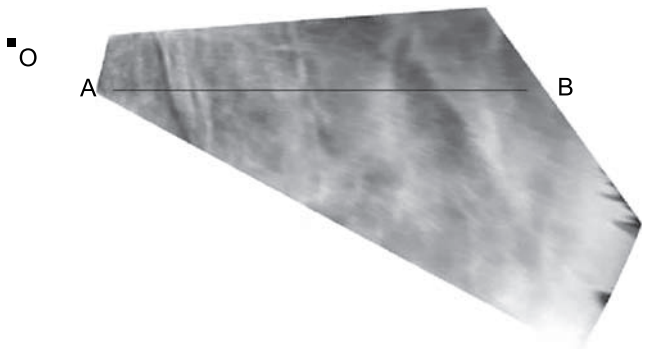

Figure 6. Projection of the emissive layer observed from Château-Renard during the night of 11–12 July 2002 from 2115 to 0030 UT. Distance AB = 600 km.

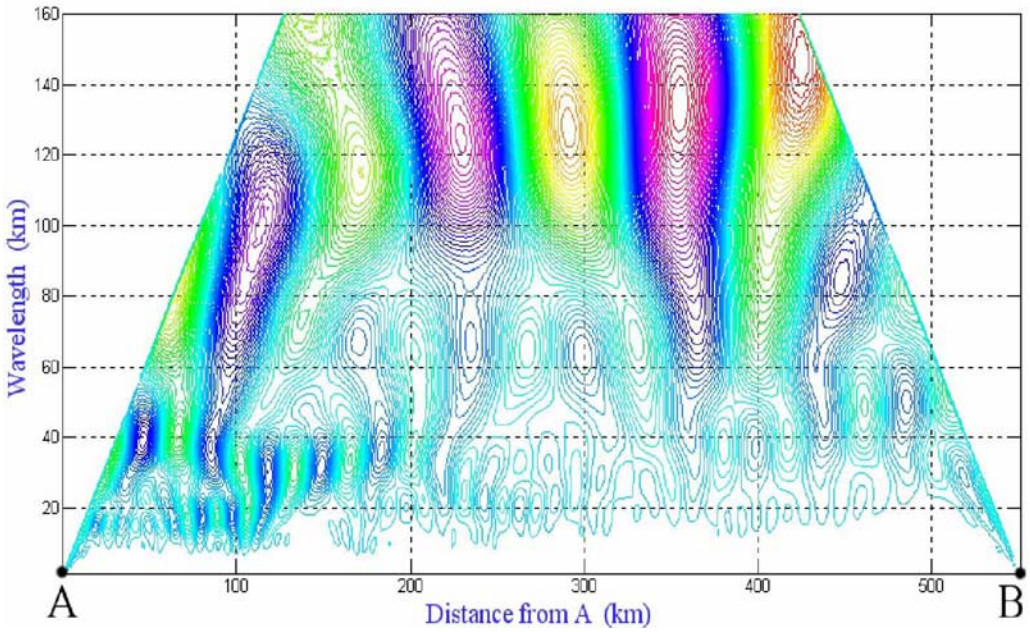

Figure 7. Wavelet transform of the spatial intensities measured on the AB projection line of Figure 6 (night 11–12 July 2001, 2115 to 0030 UT).

ing station is located at point O. The horizontal FOV is 34°. The azimuth and elevation angles of the central line of sight are 48° and 18°. The two analyses are performed for the AB line.

[15] Using the data from the image in Figure 6, a spatial frequency map of the AB segment is generated in Figure 7. Figure 7 gives the horizontal wavelengths for the various points along the AB line. Short wavelengths, in the 20–40 km range are clearly detected between A and A + 200 km. Longer wavelengths, in the 100–150 km range, are detected between A + 100 km and A + 450 km.

[16] A series of 52 photographs of the same area, taken regularly at 3 min intervals, is used to draw a map of the temporal frequencies (Figure 8). This map shows a large range of dominant periods with the smallest values being ~13 min.

[17] The results presented here compare favorably with the analyses made by other authors. During the ALOHA campaign, *Taylor et al.* [1995], *Hecht and Walterscheid* [1988], *Swenson et al.* [1995b] and *Isler et al.* [1997] found wavelengths between 10 and 53 km which are comparable to our measurements. *Nakamura et al.* [1999, 2004] reported the following values: horizontal wavelengths of 5–60 km, time periods of 5–30 min and horizontal phase speeds of 0–100 m/s.

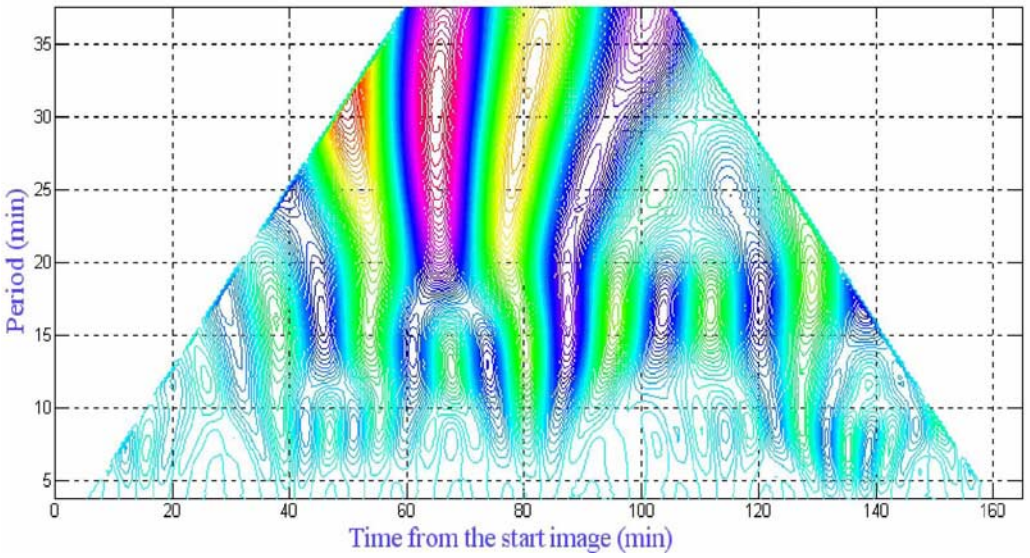

Figure 8. Wavelet transform of the temporal intensities measured in a series of photographs taken regularly every 3 min (night 11–12 July 2002, 2115 to 0030 UT).

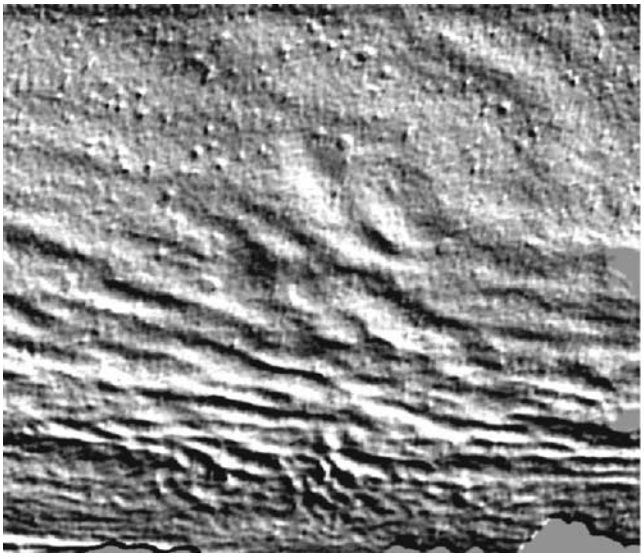

Figure 9. Image processed by a gradient filter to produce a pseudo-relief effect, 10–11 July 2002, 0016 UT. Azimuth = 270°, and elevation angle = 15°. This image is the same as in Figure 1 (right).

2.4. Pseudorelief Images of the Emissive Layer

[18] The wavy structures that appear in Figures 1 and 2 can be enhanced using image processing. Two types of pseudorelief images are produced in which the emissive layer exhibits a corrugated aspect with apparent height variations.

[19] First, Figure 9 shows the near-IR image of Figure 1 (right) (10–11 July 2002, 0016 UT) processed with a gradient filter operator. In the lower part of the image, the contour line of the Alps summits is underlined. Although the contrast is low, the gradient operator provides an image where the waves show a pseudo-relief. This operator is a (5 × 5) filter having a privileged direction that is chosen according to the direction of the structures. For instance, if the structures are horizontal, the (5 × 5) matrix will be constituted of five identical columns

$$\begin{bmatrix} -2 & -1 & 0 & 1 & 2 \\ -2 & -1 & 0 & 1 & 2 \\ -2 & -1 & 0 & 1 & 2 \\ -2 & -1 & 0 & 1 & 2 \\ -2 & -1 & 0 & 1 & 2 \end{bmatrix}.$$

If the structures are oriented at 45°, the (5 × 5) matrix will be:

$$\begin{bmatrix} 0 & 0 & 1 & 2 & 2 \\ 0 & 0 & 0 & 1 & 2 \\ -1 & 0 & 0 & 0 & 1 \\ -2 & -1 & 0 & 0 & 0 \\ -2 & -2 & -1 & 0 & 0 \end{bmatrix}.$$

[20] Second, in Figure 10 (18–19 May 1998, 2130 UT), a perspective representation of an image of an horizontal sector of 19.5° also shows a pseudo-relief. This kind of picture is quite useful as a visualization of the horizontal propagation of the wave system. A short video sequence built with successive images of the same FOV shows the direction of propagation (Animation 1).

[21] The various images previously presented show evidence of waves propagating through the emissive layer. Since the mesosphere is a chemically active region, we now consider the relative importance of chemical and dynamical processes in this region.

3. Impact of Dynamical and Chemical Processes on the Layer Altitude

[22] Shortly after the OH emission was discovered by *Meinel* [1950] and identified by *Herzberg* [1951], the altitude measurements of the emissive layer became the subject of numerous observations by ground-based [*Packer*, 1961] and rocket-borne instruments [*Packer*, 1961; *Baker and Waddoups*, 1967]. In their extensive review of 34 rocket measurements, *Baker and Stair* [1988] recommended the following numbers to be used: 86.8 ± 1.6 km for the altitude and 8.6 ± 3.1 km for the thickness of the OH emission layer. More recently, *Zhang and Shepherd* [1999] have given a concise report of the OH emission profile measured by

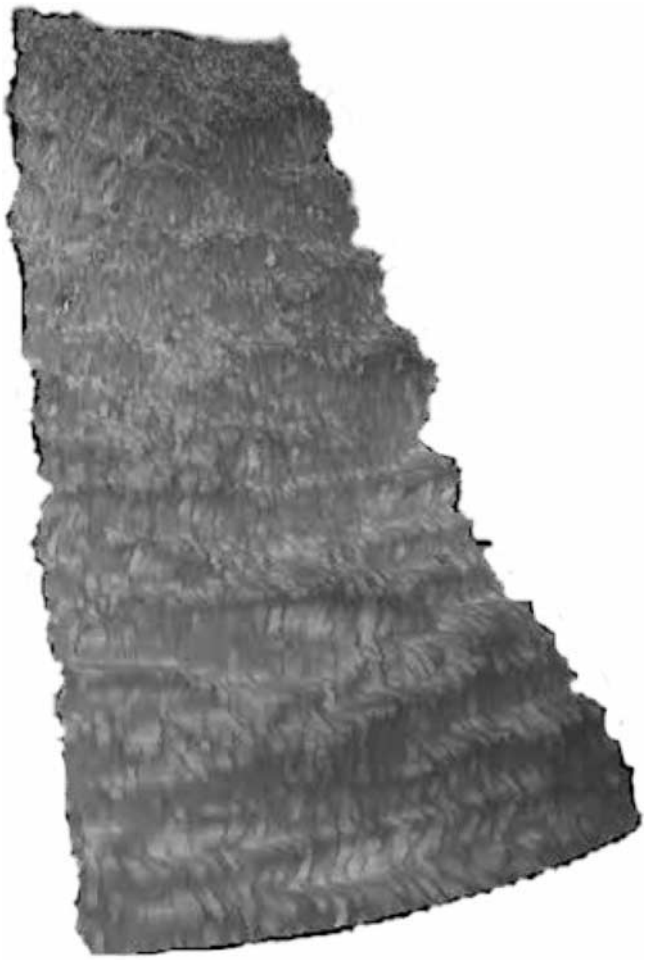

Figure 10. Sea-surface type image of the emissive layer, producing a pseudo-relief effect, 18–19 May 1998 at 0120 UT taken from the Crêt Monniot in the Jura, France, 6°24′E, 47°01′N.

WINDII on UARS [*Shepherd et al.*, 1993]. Their data are global and cover the (−40°, +40°) latitude range during the March–May 1992 and December 1992 to February 1993 periods. Their results show that the peak altitude is quite stable at between 86 and 88 km, except at the equator. They concluded that the global airglow data (OH and O^1S) provided by WINDII can improve the understanding of the tidal influence on the emissions and the differing altitudes of the layers. Vertical profiles of the OH mesospheric layer are expected to become available in the near future from measurements of the SCIAMACHY instrument on ENVISAT. New global measurements of the OH rotational temperature obtained from this instrument have recently been published [*von Savigny et al.*, 2004].

[23] The vertical profile of OH* can be calculated with a photochemical model. The production mechanism that is now generally accepted is the hydrogen-ozone reaction first proposed by *Bates and Nicolet* [1950]. The OH* radical is produced in 10 vibrational levels $\upsilon = 0,., 9$ in the hydrogen-ozone reaction. When a steady state for the different OH_υ populations is reached, the local volume emission rate at a given altitude for the various (υ', υ'') bands may be calculated using the following chemical scheme

$$\text{Production reaction} \qquad H + O_3 \rightarrow OH^* + O_2 \qquad k_1 \tag{3}$$

$$\text{Natural radiation} \qquad OH^*_{\upsilon'} \rightarrow OH^*_{\upsilon''} + h\nu(\upsilon' \rightarrow \upsilon'') \qquad A_{\upsilon'\upsilon''} \tag{4}$$

$$\text{Reaction with O} \qquad OH^* + O \rightarrow H + O_2 \qquad k_2 \tag{5}$$

$$\text{Quenching by air} \qquad OH^*_{\upsilon'} + M \rightarrow OH^*_{\upsilon''} + M \qquad k_3 \tag{6}$$

$$\text{Reaction with } O_3 \qquad OH^*_{\upsilon'} + O_3 \rightarrow HO_2 + O_2 \qquad k_4 \tag{7}$$

[24] In equation (4), $A_{\upsilon\upsilon'\upsilon''}$ is the absolute transition probability (s^{-1}) for the (υ', υ'') band. The branching ratio for producing $OH^*_{\upsilon'}$ in the H-O_3 reaction is labeled $\alpha_{\upsilon'}$.

[25] The chemical scheme for producing and destroying OH* in the υ vibrational state has been the subject of an extensive study by *McDade et al.* [1987] and *McDade and Llewellyn* [1987] in order to analyze simultaneous rocket measurements of the emission profiles of the OH (8,3) band and the $\Delta\upsilon = 2$ sequence. In their analysis, these authors introduce the concept of a "reduced kinetic parameter" that is the ratio of a kinetic constant to the absolute transition probability for a υ level, i.e., for instance, k_2/A_9 where $A_9 = \sum_{\upsilon''=0}^{8} A_{9\upsilon''}$. The reduced kinetic parameter is expressed in units of cm^3 $molecule^{-1}$. The reason for this transposition is that the kinetic equations may be established without knowing the numerical values of, for instance, k_2 and A_9. In their effort to interpret the volume emission profiles retrieved from the rocket measurements, *McDade et al.* [1987] consider two cases that depend upon the kind of collisional deactivation assumed. In the first case, during a quenching process the total vibrational energy is assumed to be removed. In the second case, called "collisional cascade," a quenching collision results in a single vibrational level jump, from level υ' to $\upsilon' - 1$. The vertical profiles of the (8, 3) band emission rate calculated using both quenching processes are compared with the profile measured by the ETON 5 rocket experiment (their Figure 4). The differences between both calculated profiles are negligible. Calculated and measured profiles for the 1.61 μm emission rate are compared in their Figure 7. Both calculated profiles are close to one another, and show a peak at 91–93 km, but do not reproduce the experimental profile that shows two distinct peaks at 88 and 99 km. Another important analysis of the hydroxyl airglow profiles is given by *Melo et al.* [2000]. The data come from the WINDII-UARS instrument. They show that the (8,3) volume emission rate generally has a maximum located between 85 and 90 km. In their model calculation, these authors use the $A_{8\upsilon''}$ transition probability values of *Mies* [1974].

[26] In order to give a tentative answer to the question related to the altitude of the layer centroid, a recent version [*Faivre et al.*, 2003b] of the model developed by *Moreels et al.* [1977] is employed. Here, the goal is not to proceed with a detailed analysis of the chemical processes comparable to the one of *McDade et al.* [1987] but rather to show the influence of dynamical processes such as gravity waves and tides.

[27] In a first run, the model only includes chemical and diffusive processes. The chemical scheme for computing the OH* profile consists of the five equations (3)–(7). The production mechanisms for the OH_υ population consist of formation by the hydrogen–ozone reaction, preferentially in the 7, 8 and 9 levels, and radiative cascade from upper vibrational levels. The loss processes are radiative cascade to lower levels and collisional deactivation or reaction with O, O_3, O_2 and N_2. The destruction reaction by O and O_3 appears much less efficient in the 75–95 km range than quenching by air. In the present study, the collision of an OH^*_υ radical with an O_2 or N_2 molecule is assumed to result in a total removal of vibrational energy. The impacts of collisional deactivations by O_2 and N_2 are considered to be identical since the results obtained by *McDade and Llewellyn* [1987] for the two collisional deactivation processes were found to similar. Under these assumptions, the intensity in a (υ', υ'') band is given by equation (8)

$$\begin{aligned} I_{em}(\upsilon', \upsilon'') &= A_{\upsilon'\upsilon''}[OH_{\upsilon'}] \\ &= A_{\upsilon'\upsilon''} \frac{\alpha_{\upsilon'} k[H][O_3] + \sum_{j=\upsilon'+1}^{9} A_{j\upsilon'}[OH_j]}{k_2[O] + k_3[M] + k_4[O_3] + \sum_{k=0}^{\upsilon'-1} A_{\upsilon' k}} \end{aligned} \tag{8}$$

[28] In this equation, the quantities between brackets are concentrations, i.e., numbers of molecules per unit volume. $A_{\upsilon'\upsilon''}$ is the absolute transition probability (s^{-1}) for the (υ', υ'') band. We use the same set of $A_{\upsilon'\upsilon''}$ values as *Melo et al.* [2000]. These values, taken from *Mies* [1974] correspond to short radiative lifetimes comprised between 3 ms ($\upsilon = 9$) and 50 ms ($\upsilon = 1$). The comparison of $A_{\upsilon'} = \sum A_{\upsilon' k}$ and $k_3[M]$ in the denominator of equation (8) implies that k_3 should have a value $\sim 10^{-12}$ cm^3 s^{-1}. *Llewellyn et al.* [1978], in a previous study of the quenching of OH* using the Mies values, suggested a k_3 of 5.8×10^{-12} cm^3/s. In the present study, three different quenching rates were

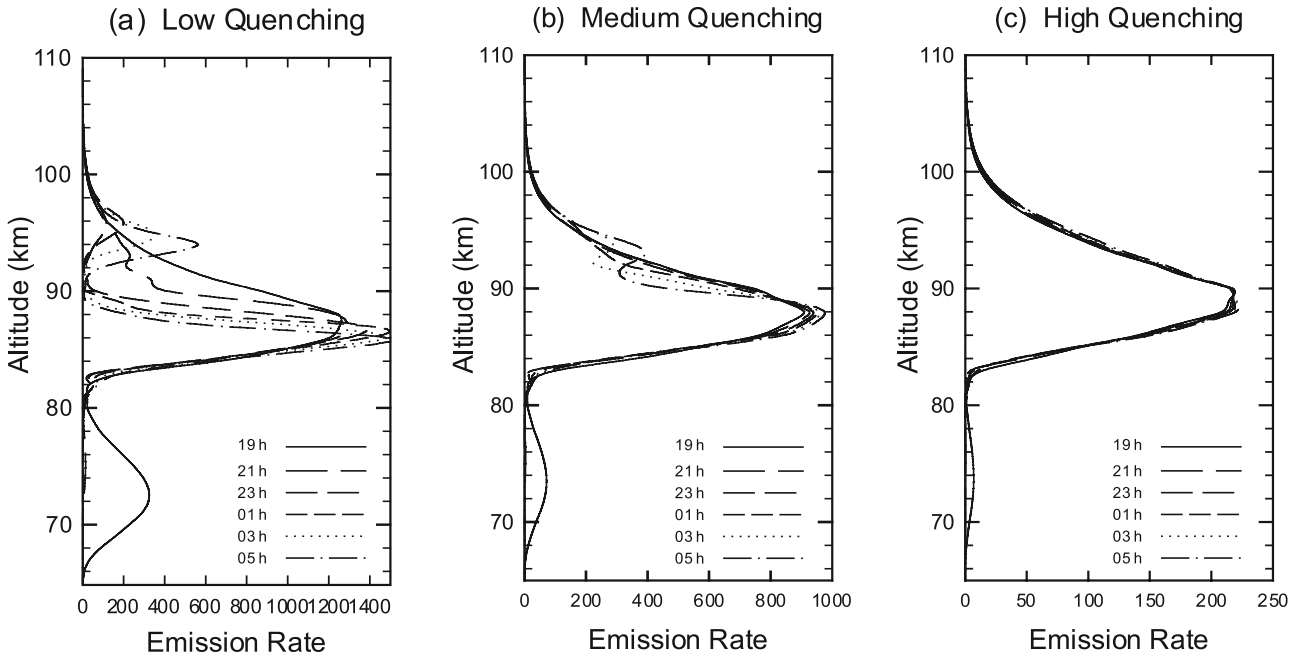

Figure 11. Vertical profile of the $OH_{v'=4}$ concentration as a function of time during the night for three different values of the quenching coefficient: (a) low, (b) medium, and (c) high. The altitude is given by the vertical axis (65–110 km). The intensity scale (horizontal axis) is relative but is the same for the three graphs.

considered: a low k_3 of 5×10^{-14} cm^3/s, a medium k_3 of 5×10^{-13} cm^3/s, and a high k_3 of 5×10^{-12} cm^3/s. The nighttime emissive layer profile and its evolution during the night is presented in Figure 11 for different values of the quenching rate. When the high 5×10^{-12} cm^3 s^{-1} value is used, the emission is found to be four or six times weaker than with the medium or low k_3 values. The altitude of the layer maximum is 89 km for the high quenching, 87.7 km for the medium quenching and, for the low quenching case, 87 km at the beginning and 86 km at the end of the night. In addition, it may be seen in Figure 11 that, with the 5×10^{-14} cm^3/s value, the emissive layer splits into a lower layer and an upper secondary layer after 4 to 5 hours from the beginning of the night. Although this is a result of the evolution of the chemical species with respect to time during the night, it might contribute, together with wave action, to produce a lamellar structure in the emissive layer as was suggested by *Melo et al.* [2000].

[29] A wave-induced perturbation in atmospheric density is now introduced into the model. Such a wave has been modeled by *Gardner and Shelton* [1985] and *Swenson and Gardner* [1998] for an isothermal atmosphere at mesospheric levels. When the mean winds are zero and the wind perturbations are created by a single monochromatic wave corresponding to a gravity wave [*Swenson and Liu*, 1998], the perturbed density is given by equation (9):

$$[M] = [M]_u \left(1 + \varepsilon e^{\beta(z-z_{OH})} \cos[\omega t - kx + m(z - z_{OH})]\right) \quad (9)$$

[30] In equation (9), z_{OH} is the altitude of the layer average centroid, $m = 2\pi/\lambda_z$ is the vertical wave number, λ_z is the vertical wavelength, $\omega = 2\pi/T$ is the intrinsic frequency, T is the period, $\beta = 1/(2H)$ where H is the atmospheric scale height, and ε is the amplitude of the modulation at the altitude z_{OH}, $(0 < \varepsilon < 1)$.

[31] In the simulation, the values for the vertical wavelength λ_z and the temporal period T are chosen by considering the results obtained during two coordinated nightglow and air density campaigns conducted in July 2000 and July 2001 [*Faivre et al.*, 2003b]. During these campaigns a Rayleigh lidar measured the atmospheric density with a 1-hour time resolution, at altitudes of 65, 70 and 75 km vertically above the Haute-Provence observatory (OHP). During the night, images of the mesospheric layer were taken from Château-Renard. The field of view included the area above OHP. During the correlated observation period, a phase-shifted variation was found between the OH intensity and the atmospheric density measured in the 72.5–78 km altitude range. The OH nightglow showed a minimum around midnight followed by an increase until the end of the night. The respective variations were $\Delta I_{OH}/I_{OH} \sim -33\%$ and $\Delta[M]_{75}/[M]_{75} \sim +25\%$. Comparable coordinated measurements of air density and OH nightglow were published by *Takahashi et al.* [2002]. In our case, because of the low density at 87 km, the Rayleigh lidar could not provide observational values with a time resolution of 1 hour at those altitudes. Consequently, in the calculation of the altitude and thickness of the emissive layer, the values λ_z = 15 and 30 km and T = 4 hours were adopted in agreement with the coordinated OH intensity-air density observations by *Faivre et al.* [2003b]. These values, lying within the allowed range of gravity wave parameters, allow us to take into account a phase-shifted variation of the OH intensity (typically a pronounced minimum around midnight) and also of the air density in the 72.5–78 km altitude range. In the model calculation, the upward propagating density wave is assumed to have an amplitude of 15% at

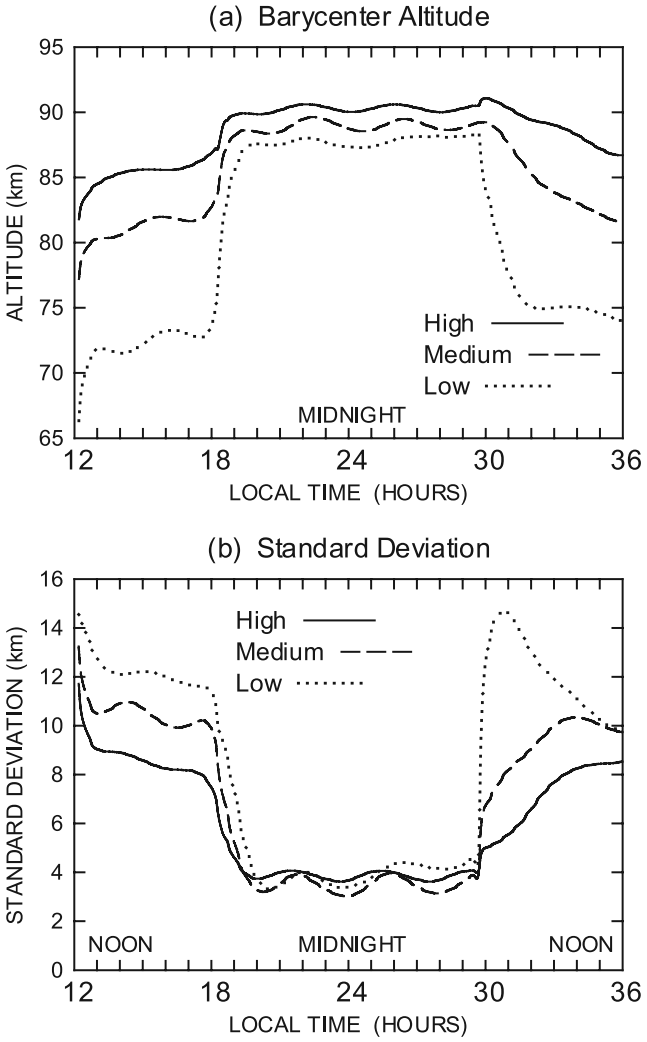

Figure 12. Variation as a function of time of (a) the altitude of the emissive layer barycenter and (b) the altitude mean deviation that is approximately half of the layer thickness. In this simulation, a density wave having a modulation factor of 15% and a vertical wavelength λ_Z = 15 km propagates vertically with a temporal period T = 4 hours. Three quenching rate values are chosen: high $k_3 = 5 \times 10^{-12}$ cm^3/s (solid line), medium $k_3 = 5 \times 10^{-13}$ cm^3/s (dashed line), and low $k_3 = 5 \times 10^{-14}$ cm^3/s (dotted line).

75 km. It is represented by equation (9) where the amplitude increases exponentially with a factor $\beta = 1/(2H)$. Figures 12a and 12b present, for λ_z = 15 km, the evolution with time of the altitude of the layer barycenter and of its mean deviation, which is about half of the layer thickness. The barycenter altitude is modulated as a result of the density wave perturbation. The centroid altitude increases with the quenching coefficient. The amplitude of the altitude oscillation $z_{max} - z_{min}$ is ~0.8 km, ~1.2 km and ~0.8 km respectively for the high, medium and low k_3 values. In Figure 12b, it is shown that the layer thickness is also modulated with the same temporal period of 4 hours. The layer thickness is ~7 km for all values of k_3.

[32] In Figures 13a and 13b the density wave is assumed to have a vertical wavelength λ_z = 30 km and an amplitude of 15% at 75 km. The altitude modulation is larger than for the λ_z = 15 km case. The $z_{max} - z_{min}$ difference is ~0.8 km, ~1.3 km and ~1.8 km respectively for the high, medium and low k_3 values. The layer thickness is ~7 km again for all values of k_3 as for the λ_z = 15 km case. When Figures 12a and 13a are compared, it should be noted that the phase of the altitude modulation is different in both figures because the vertical wavelength is different.

[33] The calculated altitude of the layer centroid is higher when adopting a higher quenching rate because the emissive layer is strongly eroded at its lower side. Considering that the experimentally measured altitudes of the layer are comprised between 86 and 88 km [*Zhang and Shepherd*,

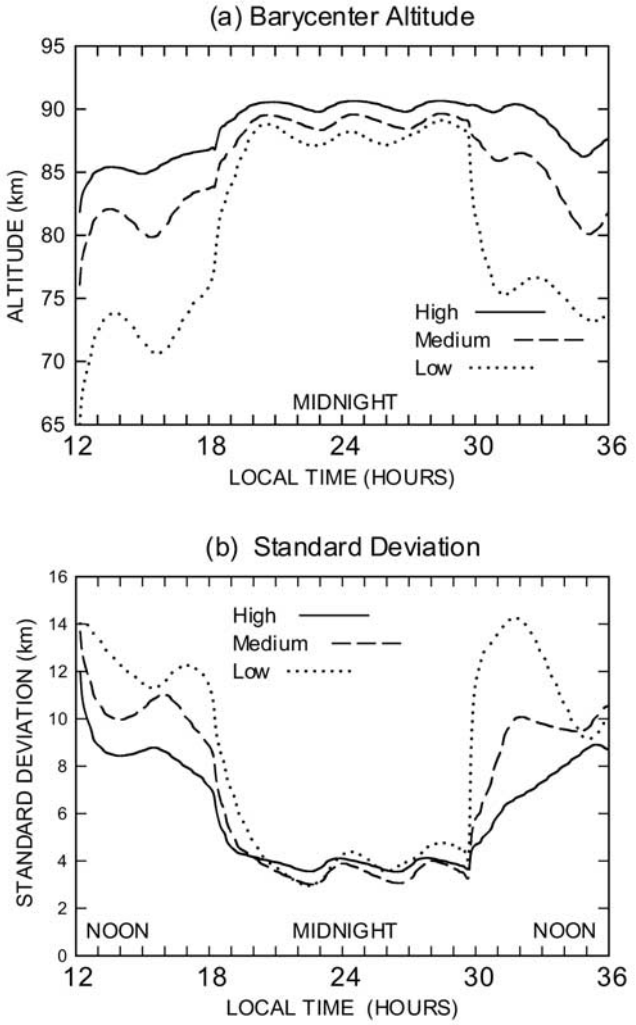

Figure 13. Variation as a function of time of (a) the altitude of the emissive layer barycenter and (b) the altitude mean deviation that is approximately half of the layer thickness. In this simulation, a density wave having a modulation factor of 15% and a vertical wavelength λ_Z = 30 km propagates vertically with a temporal period T = 4 hours. Three quenching rate values are chosen: high $k_3 = 5 \times 10^{-12}$ cm^3/s (solid line), medium $k_3 = 5 \times 10^{-13}$ cm^3/s (dashed line), and low $k_3 = 5 \times 10^{-14}$ cm^3/s (dotted line).

1999], we suggest that a quenching rate of 2 to 5 $\times$ 10^{-13} cm^3/s can possibly be used in photochemical calculations comparable to those presented here. Having simulated the influence of the propagation of a density wave on the altitude of the barycenter and the thickness of the emissive layer, additional information about the dynamical processes prevailing in the mesosphere can be derived from the images obtained with the CCD cameras.

4. Stereoscopic Observations

[34] It has been shown in Figure 11 of the previous section that the barycenter altitude of the OH mesospheric emissive layer is between 85 and 90 km, depending on the quenching value, this even though the medium has no contour, nor any discontinuous surface. The standard deviation σ is $\sim$3.5 km (Figure 12b). The photochemical model showed that the propagation of a density wave with a modulation coefficient ε = 15% results in a modulation of the altitude of the layer barycenter with an amplitude of 0.8 to 1.8 km. Using efficient image processing and stereoscopic techniques, it should be possible to obtain, from measurements, a surface map of the mesospheric emission layer barycenter altitude. The objective of the analysis in this section is to provide a view of the layer that might exhibit a corrugated structure with height variations not too dissimilar to what has been indicated above.

4.1. Stereocorrelation Method

[35] A stereocorrelation method is used in an attempt to obtain a surface map representation of the altitude of the emissive layer barycenter from satellite-type images as produced in section 2. Stereoscopy or stereovision [*Faugeras*, 1993; *Hartley and Zisserman*, 2004] is based on the principle that information about surface depth can be retrieved by triangulation using two images having a common zone in their field of view. A brief account of the stereoscopic method is given below. This method was used by *Störmer* [1910, 1911] as soon as the sensitivity of photographic plates became sufficient to take pictures of the aurora. He published a table of auroral altitudes comprised between 40 and 280 km, each altitude being dependent on the type of aurora: drapery, rays etc. Triangulation was employed by *Belon et al.* [1966] to measure the height and vertical extent of aurorae. Using a rocket with a trajectory in the meridian plane together with three photometers along the same north-south line, *Vallance-Jones et al.* [1991] obtained excellent profiles of the N_2^+ and O^1S that were used for analyzing the mechanisms involving energetic electrons.

[36] Figure 14 shows the image planes of two cameras constituting a stereoscopic vision system [*Ma et al.*, 2004, p. 111]. The camera lens optical centers C_1 and C_2 are shown behind the image planes for clarity, but they actually are located in front of these planes. In order to calculate the 3-D position of the point *P*, it is first necessary to recognize that, in both images (IM1) and (IM2), the points p_1 and p_2 correspond to the projections of the same physical point *P*. Thus the critical phase consists in establishing correspondences between pairs of points, or point matching. Then, the equations of the lines $C_1\,p_1$ and $C_2\,p_2$ can be used to obtain the coordinates of the intersection point *P*. In order to make

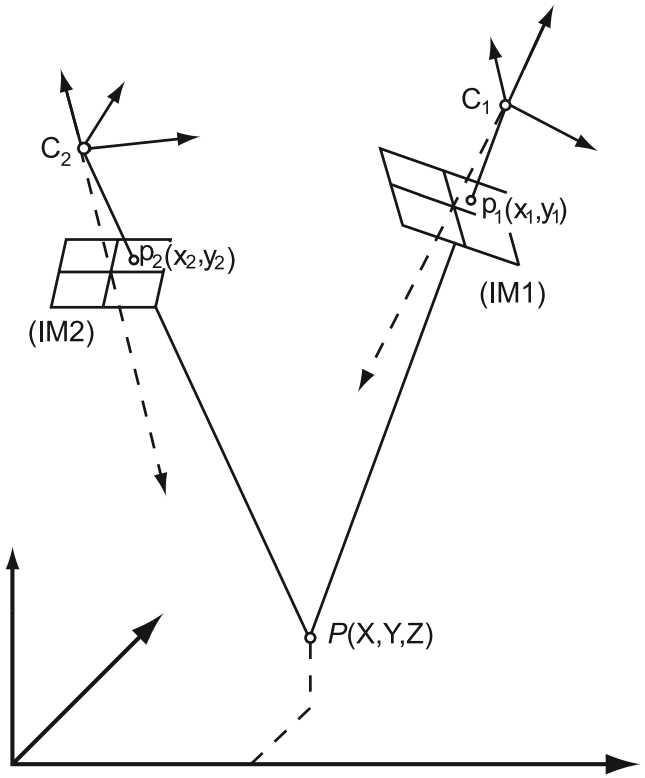

Figure 14. Principle of stereovision. C_1 and C_2 are the optical centers of two cameras. The image planes are (IM1) and (IM2) and are shown in front of C_1 and C_2 for clarity. Given a point p_1 in the image plane (IM1), the problem consists in finding the matching point p_2 in (IM2). When p_2 is located, the coordinates of *P* are found in using the equations of the lines C_1P_1 and C_2P_2 The plane defined by the three points C_1PC_2 is called the epipolar plane. The intersections of the (C_1 C_2) line with the image planes are called epipoles. The intersection of the epipolar plane with the image plane is called epipolar line.

a rational and constrained search for the correlated pixels, the intrinsic parameters (focal length of the lens, size of pixels) of both cameras, as well as their orientation and position relative to each other, must be known.

[37] To find the matching pixel p_2 in the image (IM2) of a pixel p_1 in image (IM1), a geometrical constraint called ''epipolar constraint'' is used. This important property induced by the geometry of the stereosystem drastically reduces the area of potential matching. Let us define the plane C_1PC_2 as the ''epipolar plane'' related to the physical point *P*. The intersection of this plane with the image plane (IM2) is the epipolar line related to the point p_1.

[38] An additional criterion must be used to locate precisely the matching point p_2 on the epipolar line. In the case of a delimited object (a box for instance), a well-defined point (a corner) or a line (a side) may be used. In our case, as the object is diffuse, we use the normalized cross correlation (NCC) criterion [*Ma et al.*, 2004, p. 89]. Two small windows are defined around the p_1 point and the p_2 matching point that we try to locate in the (IM2) plane. A function, defined by equation (10), is used to calculate an

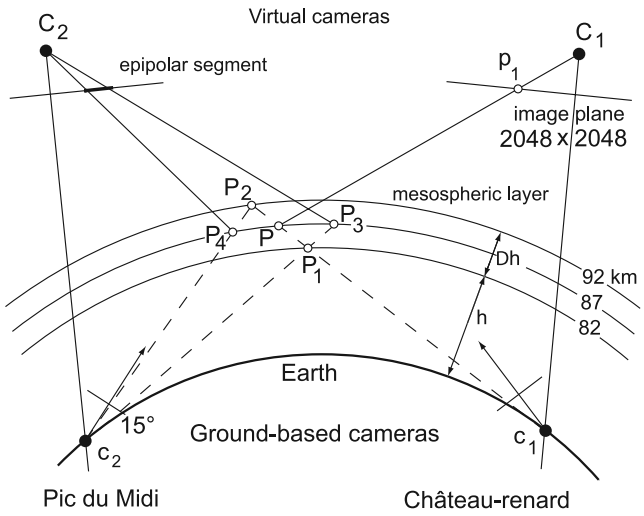

Figure 15. Determination of the matching point of a point p_1 in the image plane of the virtual camera C_1. The altitude of the barycenter of the emissive layer is assumed to be comprised between 82 and 92 km according to *Baker and Stair* [1988] and *Melo et al.* [2000].

intercorrelation coefficient called the NCC parameter whose value is comprised between −1 and +1:

$$NCC(x, y, dx, dy) = \frac{\sum_{k=-p}^{p}\sum_{l=-p}^{p}(I_1(x+k,y+l)-\bar{I}_1)\left(I_2\left(x+d_x+k,y+d_y+l\right)-\bar{I}_2\right)}{\sqrt{\sum_{k=-p}^{p}\sum_{l=-p}^{p}(I_1(x+k,y+l)-\bar{I}_1)^2}\sqrt{\sum_{k=-p}^{p}\sum_{l=-p}^{p}\left(I_2\left(x+d_x+k,y+d_y+l\right)-\bar{I}_2\right)^2}} \quad (10)$$

[39] A value of +1 for the NCC parameter implies a perfect match. In equation (10), $I_1(x, y)$ and $I_2(x + d_x, y + d_y)$ are the intensities at the matched points p_1 and p_2. The coordinates (x, y) of the pixels of the image I_1 are relative to the frame defined by the virtual image plane associated with the Château-Renard camera, with the origin located in the top right corner. The x axis is defined by the eastern direction and the y axis follows the southern direction. The projection frame is a 2048 × 2048 pixel image. The coordinates of the pixels in the image I_2 are relative to the frame defined by the virtual image plane associated with the Pic du Midi camera. A square window of dimensions $(2p + 1, 2p + 1)$ is defined around the points p_1 and p_2. $\overline{I_1}$ and $\overline{I_2}$ are the respective intensities averaged over the $(2p + 1)^2$ pixels of the windows. As the position of p_2 is the result of an iteration, k and l represent increments related to the (x,y) and $(x + d_x, y + d_y)$ coordinates of both points. In our case, the adopted correlation size was 13x13 pixels, which is small enough to discriminate the wave structures. In addition, the NCC has the advantage of being insensitive to the difference in contrast between the images. It is relatively robust for the process of finding the structural correspondence. Finally, another constraint used in our application is to check the monotonic order of the disparity vector. This means that, for a pixel p_1' located at an abscissa greater than the abscissa of pixel p_1 in the right image, the matched pixel p_2' should also be at an abscissa greater than pixel p_2 in the left image.

[40] Figure 15 serves to illustrate the determination of the epipolar segment line, on the left-hand virtual image plane, associated to a point in the other virtual image plane. The altitude of the C_1 and C_2 points are set to 500 km. The geometry makes use of the two virtual camera frames, the two real cameras frames and also of the thickness of the layer, which is assumed to be equal to 10 km [*Baker and Stair*, 1988; *Melo et al.*, 2000]. Both virtual cameras look down upon the emissive layer as if it was at an altitude of 87 km. In Figure 15, let p_1 be a pixel in the virtual camera 1. The line of sight defined by the current pixel p_1 and the virtual optical center C_1 intersects the 87 km layer at a point called P. The spatial point P when looked from the real camera has two conjugate points P_1 and P_2 located respectively at 82 and 92 km. Those spatial points can be projected from the left-hand real camera onto the 87 km layer in two points called P_3 and P_4. Finally, the projection of those two points onto the left-hand virtual image plane defines a segment line, so-called epipolar line. The epipolar line is the interval of possible pixels in the left image that can potentially be matched with the starting pixel in the right-hand virtual image plane. The epipolar line of a pixel is determined only under the constraint of the stereoscopic geometry of the system. This process is repeated for each pixel of the region of interest. Even though the lines of sight of the virtual cameras may be slanted relative to the layer, the images do not contain any change in intensity related to the view angle as the Van Rhijn effect from the original ground-based images was removed and no related effect was reintroduced in the final images.

[41] Simultaneous observations of the mesospheric emissive layer were conducted with two cameras at the Pic du Midi (Hautes-Pyrénées) and Château-Renard (Hautes-Alpes) observatories. The fields of view were set up in a "vis à vis" configuration. The azimuths of the median line of sight of both cameras were respectively set at 249° and 69°, i.e., in opposite directions. The elevation angle for both cameras was 15°. The geometric configuration of the respective fields of view, projected on an horizontal plane is shown in Figure 16.

4.2. First Results of Stereoscopic Observations

[42] Preliminary results obtained in using a pair of images simultaneously taken at the Pic du Midi and the Château-Renard observatories during the night of 8–9 September 2000 are presented in this section. Three square surfaces having an area between 40 × 40 and 50 × 50 km^2 are chosen at three different locations inside the common zone of the field of view of both cameras (Figure 16). These emissive layer parcels are depicted in surface map representations in Figures 17–19. Figures 17b, 17c, 18b, 18c, 19b and 19c show intensity maps simultaneously measured at Château-Renard and at Pic du Midi. The images taken at Pic du Midi were more noisy than the images taken at

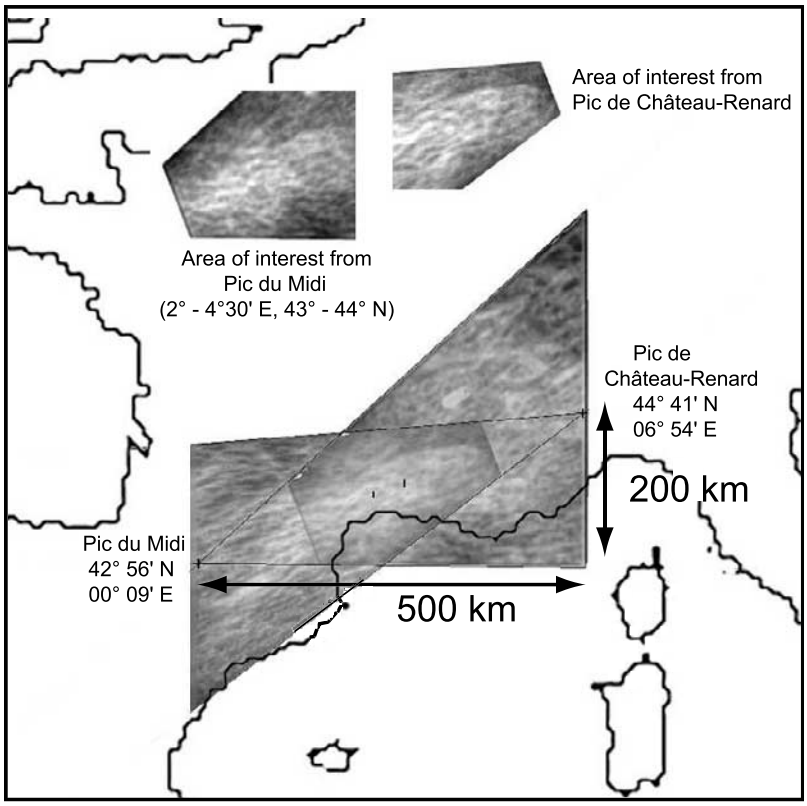

Figure 16. Horizontal projection of the fields of view of both cameras located at the Pic du Midi (left, looking to the right) and at Château-Renard (right, looking to the left). Both views were simultaneously taken on 8–9 September 2000 at 0123 UT.

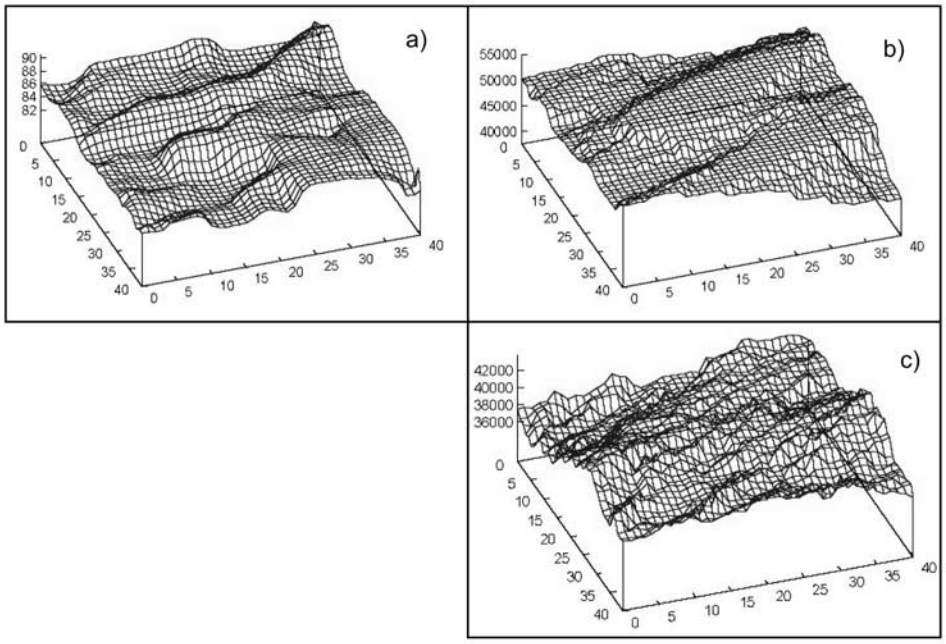

Figure 17. Barycenter geometric altitude and intensity surface maps of a 40 × 40 km^2 area of the mesospheric layer from images taken during the night of 8–9 September 2000 at 0117 UT. (a) Stereoscopic 3-D reconstitution of the layer centroid altitude. The vertical scale is 82–92 km. (b) Intensity map measured from Château-Renard. (c) Intensity map measured from Pic du Midi. The vertical scales in Figures 17b and 17c are identical. They give the local emission intensity in arbitrary, although identical units.

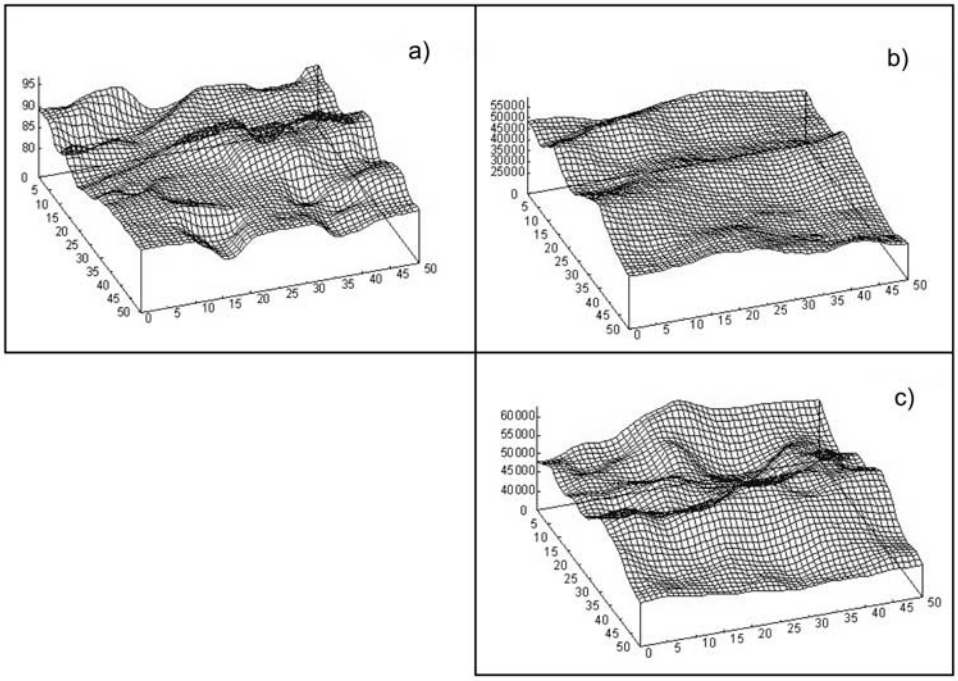

Figure 18. Barycenter geometric altitude and intensity surface maps of a 50 × 50 km^2 area of the mesospheric layer from images taken on 9 September 2000 at 0120 UT. (a) Stereoscopic 3-D reconstitution of the layer centroid altitude. The vertical scale is 82–92 km. (b) Intensity map measured from Château-Renard. (c) Intensity map measured from Pic du Midi. The vertical scales in Figures 18b and 18c are identical. They give the local emission intensity in arbitrary, although identical units.

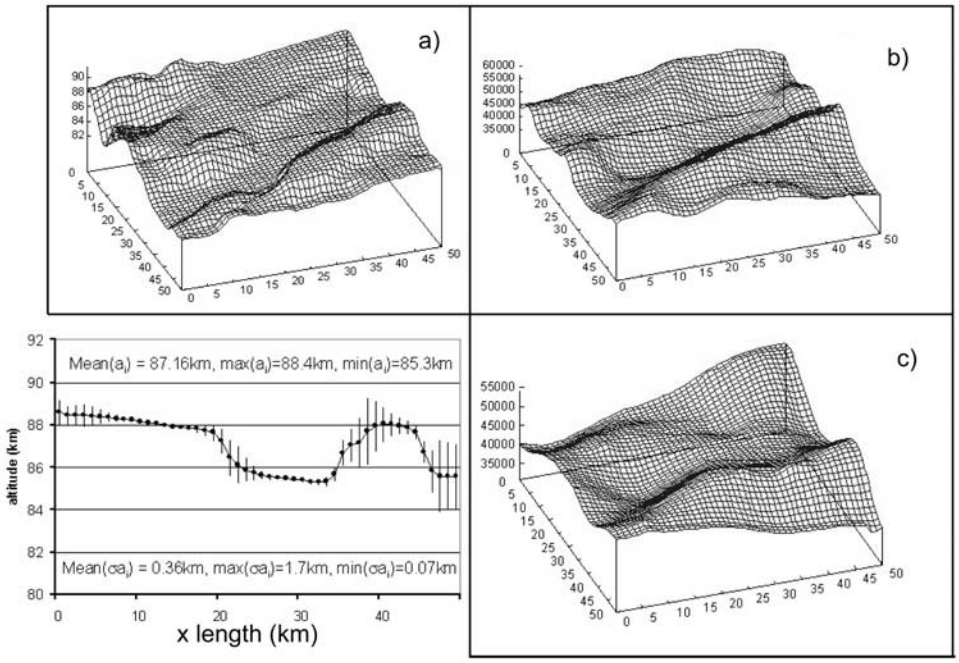

Figure 19. Barycenter geometric altitude and intensity surface maps of a 50 × 50 km^2 area of the mesospheric layer onto images taken on 9 September 2000 at 0123 UT. (a) Stereoscopic 3-D restitution of the layer centroid altitude. The vertical scale is 82–92 km. (b) Intensity map measured from Château-Renard. (c) Intensity map measured from Pic du Midi. The vertical scales in Figures 19b and 19c are identical. They give the local emission intensity in arbitrary, although identical units. Shown at the bottom left is the barycenter altitude profile along a Cartesian line.

Château-Renard, as shown in Figure 17c, where the raw intensity values are displayed. The surface maps in the Figures 18b, 18c, 19b and 19c are slightly different, most likely because of differences in the optical absorption between each camera and the common observed zone caused by the possible presence of clouds, haze or aerosol. Figures 17a, 18a, and 19a show the geometric altitude map of the emissive layer barycenter, calculated using the stereo-correlation method applied to the pair of images in Figures 17b, 17c, 18b, 18c, 19b and 19c. These figures clearly show the wavy structure of the emissive layer that appears in the intensity and in the centroid altitude surface maps. The horizontal wavelength can be easily measured as 21 km in Figures 17 and 18 and 26 km in Figure 19.

[43] The barycenter altitude map reproduces the main lines of the wavy structures present in the intensity maps. This point is quite clear in Figure 20 where Figure 20a (same as Figure 19, bottom left) depicts the centroid altitude along the Cartesian axis that is about 60° from the wave crest. The mean altitude equals 87.2 km. The maximum and minimum values along that line are, respectively, 88.4 km and 85.3 km. The amplitude of the measured altitude oscillation $z_{max} - z_{min}$ is in the range of ~1.8–2.1 km. This value, measured in a specific small area of the wave-field, may be compared with the model results (section 3) which are in the range of ~0.8–1.8 km depending upon the quenching rate and the density wave characteristics. Figures 19b and 19c present the intensity profile for the same Cartesian line in the images from Château-Renard and Pic du Midi. A comparable horizontal wavelength of ~26 km can be seen. There is an apparent shift of $\sim\lambda/4$ between the altitude and the intensity profiles.

[44] The uncertainty level on the altitudes in the surface maps in Figures 17a, 18a, 19a and 20a is given by the relative measure of the quality of pair matching. An uncertainty parameter is calculated using the correlation coefficient whose value is comprised between −1 and +1. For each correlation value between a pixel with coordinates (x, y) (in the IM1 virtual image frame) and the pixel $(x + d_x, y + d_y)$ (in the IM2 virtual image frame) (see equation (7)) we assign, in an affine way, an uncertainty parameter whose value is equal to 0 when the correlation is 1 and 10 km (the interval of layer thickness authorized) when the correlation is −1. The uncertainty parameter is not a true error bar because it does not take into account the contributions of individual sources such as the uncertainty of the intensity or possible different optical absorptions along the lines of view to both cameras. However, because of the fact that the two real cameras are used to compute the projection of the optical line issued from the current pixel (x, y) in IM1 onto the second virtual image plane (see Figure 14), the change of the layer's height projection from 87 to 85 or 89 km would not affect the uncertainty parameters of the retrieved altitudes. The consequence would instead be a slight shift (less than 2 pixels) of the epipolar segment but even this would be retrieved by the use of the actual layer's height projection in the stereoalgorithm. The other parameter which has more significance than the height of the projected layer (taken to 87 km here) in the error bar analysis is the height of the virtual cameras. The value of 500 km guarantees a good compromise of epipolar segment length (30 pixels for the interval of 82–92 km of search) and the inclusion of the common FOV in both projections. Taking a lower height for the virtual cameras could reduce the error bars, but also reduce the size of the measurement of the surface depth altitude.

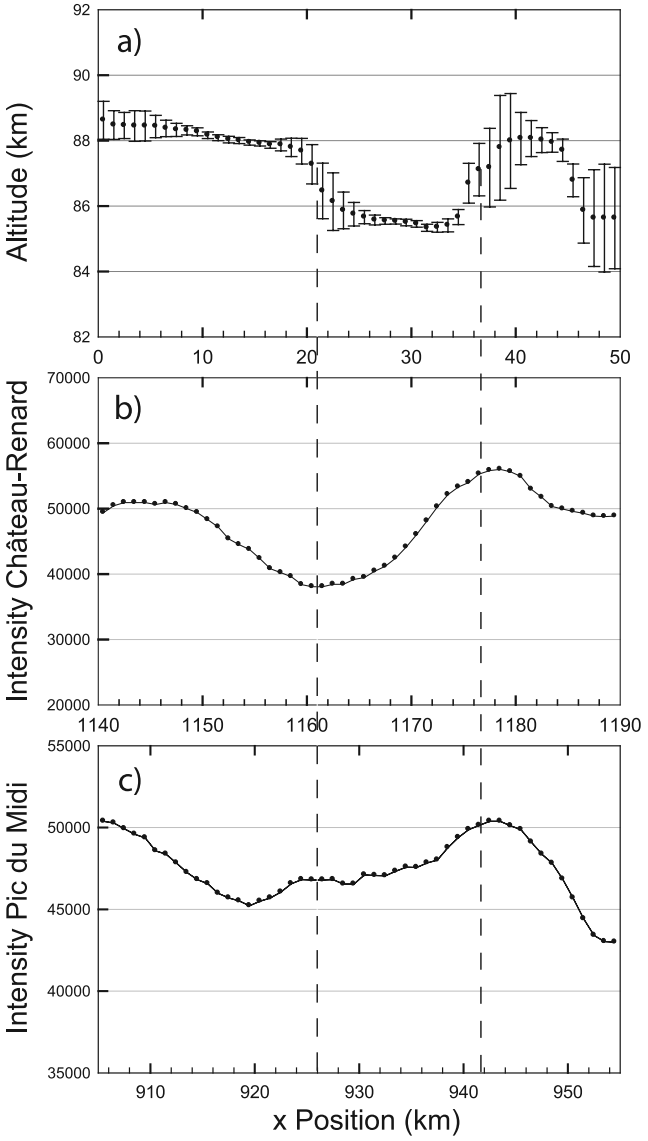

Figure 20. Cuts along a Cartesian line of the barycenter altitude and intensity 3-D views presented in Figures 19a–19c. The angle between the Cartesian line and the wave crest is ~60°. The wave structure is clearly present in the (a) barycenter altitude and (b and c) in the intensity profiles. Figure 20b is the intensity profile from the image taken at Château-Renard, and Figure 20c is the intensity profile from the image taken at Pic du Midi.

[45] The results presented here are in agreement with the global data provided by WINDII-UARS [*She and Lowe*, 1998; *Zhang and Shepherd*, 1999] and with the profiles shown in the review by *Baker and Stair* [1988]. The satellite data of the first authors show that the altitude of the OH volume emission rate peak is comprised between 86 and 88 km. The mean peak altitude reported by the second authors as a result of 34 rocket flights is 87.4 km. Our

results from stereoscopic observations provide, on a much smaller geographical scale, a more detailed description of the mesospheric emissive layer.

5. Summary and Conclusion

[46] A program aimed at providing a spatial and temporal description of the near-IR nightglow was undertaken using two CCD cameras. This program consisted in first taking a series of near-IR photographs of the sky at low elevation angle. A computer code was developed to invert the perspective effect and provide a satellite-type view of the mesospheric emissive layer. Panoramas of the sky were recorded and inverted, providing a circular view extending to distances larger than 1000 km. A wavelet spatial and temporal analysis of a series of photographs provided the parameters of the wavefield: horizontal wavelengths in the ranges of 20–40 km and 100–150 km, periods in the range of 10–40 min and a mean phase speed of ~35 m/s. These figures are consistent with the results obtained by *Turnbull and Lowe* [1991] and *Stockwell and Lowe* [2001]. These authors, using a network of three radiometers in southwestern Ontario, measured a horizontal wavelength $\lambda_h = 25$ km, a period T = 10 min and a phase speed equal to 45 m/s.

[47] Using an atmospheric chemical model including molecular and eddy diffusion, we showed that, after the evening twilight period, the populations of the OH_υ vibrational levels steadily decrease during the course of the night. The efficiency of the quenching process by air was evaluated in adopting three values for the OH* + air (3) reaction rate: a "high" k_3 of 5×10^{-12} cm^3/s, a "medium" k_3 of 5×10^{-13} cm^3/s, and a "low" k_3 of 5×10^{-14} cm^3/s. With the "high" quenching, the emission is 6 times less than with the "low" value. The altitude of the emissive layer barycenter is higher at ~89 km with the high quenching than with the low value at ~87 km. As for the layer thickness, there are no significant differences between the three cases. The model shows that the upward propagation of a density wave in the MLT region produces an oscillation in the emission intensity and in the altitude of the layer barycenter. The modulation amplitude of the layer altitude may be as large as ~0.8 to 1.8 km, depending upon the value of the quenching rate and the vertical wavelength of the density wave. This result is in agreement with the model results of *Ward* [1999] which show that the dynamical effects of the diurnal tides must be taken into account in any attempt to determine background atmospheric parameters.

[48] A new observational program aimed at obtaining a better description of the wavefield was initiated on 7–10 September 2000. Stereoscopic image pairs of the OH emission were taken simultaneously at the Pic du Midi (Hautes Pyrénées) and the Pic de Château-Renard (Hautes Alpes) observatories. The cameras, separated in distance by 570 km, operated in a "vis à vis" mode. The elevation of the lines of sight was 15° above horizon. A set of pairs of ground-based images transformed to satellite-type images was obtained. A stereocorrelation method used in 3-D vision for objects devoid of contour lines or corner points was used to retrieve surface maps of the altitude of the layer barycenter. The criterion for searching matching points consisted in calculating a normalized cross-correlation parameter defined by using the intensities of a point in a picture and of its presumed matching point in the other picture. The area of a surface map section was 50×50 km^2. Surface maps obtained during the night of 9–10 September 2000, show the presence of wave crests with the same direction as in the intensity maps. The horizontal wavelengths measured in the altitude and intensity maps of 9 September, 0123 UT have the same value of λ_h = 26 km. The amplitude of the barycenter altitude variation across the measured field of view is in the range of ~1.8–2.1 km. Given the results of the model calculations, the modulation layer may be interpreted, at least partially, by an enhancement of the quenching process giving rise to an increase in the erosion on the lower side of the layer when the air density increases as a consequence of a gravity wave propagation. This result is in agreement with the results of the OSIRIS experiment related to the variation of the OH emission measured along the orbit track of ODIN [*Llewellyn et al.*, 2003, Figure 13].

[49] The stereoscopic ground-based program presented here provides additional useful data to global satellite observations. The field of view covered when observing from the ground is obviously limited, but may be extended over ~2000 km when taking near-IR pictures at low elevation angles. Future observational campaigns will be conducted in Peru at low latitudes. We also plan to use the stereoscopic method for observing cirrus clouds in the lower atmosphere where cirrus-aerosol interactions play an important role in the atmospheric environment heterogeneous chemistry.

[50] **Acknowledgment.** Sweetest thanks are due to Marie-Jeanne for unforgettable help at Château-Renard in July 1999 and July 2001.

References

Baker, D. J., and A. T. Stair (1988), Rocket measurements of the altitude distributions of the hydroxyl airglow, *Phys. Scr.*, *37*, 611–622.

Baker, D. J., and R. O. Waddoups (1967), Rockets measurements of mid-latitude night airglow emissions, *J. Geophys. Res.*, *72*(19), 4881–4883. (Correction, *J. Geophys. Res.*, *73*(7), 2546–2547, 1968.)

Bates, D. R., and M. Nicolet (1950), The photochemistry of atmospheric water vapor, *J. Geophys. Res.*, *55*, 301–327.

Battaner, E., and A. Molina (1980), Turbopause internal gravity waves, 557.7 nm airglow, and eddy diffusion coefficient, *J. Geophys. Res.*, *85*, 6803–6810.

Belon, A. E., R. J. Romick, and M. H. Rees (1966), The energy spectrum of primary auroral electrons determined from auroral luminosity profiles, *Planet. Space Sci.*, *14*, 597–615.

Danjon, A. (1959), *Astronomie Générale: Astronomie Sphérique et Eléments de Mécanique Céleste*, pp. 143–162, J.& R. Sennac, Paris.

Degenstein, D. A., J. T. Wiensz, A. E. Bourassa, R. L. Gattinger, N. D. Lloyd, and E. J. Llewellyn (2004), The twilight flash of the OH Meinel bands in the airglow as measured with OSIRIS in ODIN, paper presented at Eur. Geophys. Soc. Meeting, Nice, France.

Degenstein, D. A., R. L. Gattinger, N. D. Lloyd, A. E. Bourassa, J. T. Wiensz, and E. J. Llewellyn (2005), Observations of an extended mesospheric tertiary ozone peak, *J. Atmos. Sol. Terr. Phys.*, *67*, 1395–1402.

Faivre, M. (2004), Etude par imagerie stéréoscopique et par interférométrie des structures dynamiques de la haute atmosphère, thèse, Université de Franche-Comté, Besançon, France.

Faivre, M., G. Moreels, D. Pautet, and J. Clairemidi (2003a), Fourier analysis of a virtual satellite view of the NIR atmospheric emission over Europe, *Adv. Space Res.*, *32*(5), 843–848.

Faivre, M., G. Moreels, D. Pautet, P. Keckhut, and A. Hauchecorne (2003b), Correlated measurements of mesospheric density and near infrared airglow, *Adv. Space Res.*, *32*(5), 777–782.

Faugeras, O. (1993), *Three Dimensional Computer Vision: A Geometric Viewpoint*, 695 pp., MIT Press, Cambridge, Mass.

Gardner, C. S., and J. D. Shelton (1985), Density response of neutral atmospheric layers to gravity wave perturbations, *J. Geophys. Res.*, *90*, 1745–1754.

Glass, I. S. (1999), *Handbook of Infrared Astronomy*, 185 pp., Cambridge Univ. Press, New York.
Haralick, R., and L. Watson (1981), A facet model for image data, *Comput. Graphics Image Processing*, *15*, 113–129.
Hartley, R., and A. Zisserman (2004), *Multiple View Geometry in Computer Vision*, 2nd ed., 672 pp., Cambridge Univ. Press, New York.
Hauchecorne, A., M.-L. Chanin, and R. Wilson (1987), Mesospheric temperature inversions and gravity wave dynamics, *Geophys. Res. Lett.*, *14*, 935–939.
Hecht, J. H., and R. L. Walterscheid (1988), A comparison of atmospheric tides from observations at the mesopause level during the ALOHA-93 with the model predictions of the TIME-GCM, *J. Geophys. Res.*, *103*, 6307–6321.
Hersé, M., G. Moreels, and J. Clairemidi (1980), Waves in the OH emissive layer: Photogrammetry and topography, *Appl. Opt.*, *19*, 355–362.
Herzberg, G. (1951), The atmospheres of the planets, *J. R. Astron. Soc. Can.*, *45*, 100–123.
Isler, J. R., M. J. Taylor, and D. C. Fritts (1997), Observational evidence of wave ducting and evanescence in the mesosphere, *J. Geophys. Res.*, *102*, 26,301–26,313.
Llewellyn, E. J., B. H. Long, and B. H. Solheim (1978), The quenching of OH* in the atmosphere, *Planet. Space Sci.*, *26*, 525–539.
Llewellyn, E. J., et al. (2003), First results from the OSIRIS instrument onboard Odin, *Publ. 92*, pp. 41–47, Sodankylä Geophys. Obs., Sodankylä, Finland.
Ma, Y., S. Soatto, J. Košecká, and S. S. Sastry (2004), *An Invitation to 3-D Vision, From Images to Geometric Models*, 526 pp., Springer, New York.
Mallat, S. (1997), *Wavelet Signal Processing*, Elsevier, New York.
McDade, I. C., and E. J. Llewellyn (1987), Kinetic parameters related to sources and sinks of vibrationally excited OH* in the nightglow, *J. Geophys. Res.*, *92*(A7), 7643–7650.
McDade, I. C., E. J. Llewellyn, D. P. Murtagh, and R. G. H. Greer (1987), Eton5: Simultaneous rocket measurements of the OH Meinel $\Delta v = 2$ sequence and (8,3) band emission profiles in the nightglow, *Planet. Space Sci.*, *35*(9), 1137–1147.
Meinel, A. B. (1950), OH emission bands in the spectrum of the night sky, *Astrophys. J.*, *111*, 555–564.
Melo, S. M. L., R. P. Lowe, and J. P. Russell (2000), Double-peaked hydroxyl airglow profiles observed from WINDII/UARS, *J. Geophys. Res.*, *105*(D10), 12,397–12,403.
Meriwether, J. W., and P. D. Dao (1994), Rayleigh lidar observations of mesosphere temperature structure, *J. Geophys. Res.*, *99*, 16,976–16,987.
Mies, F. H. (1974), Calculated vibrational probabilities of OH ($X^2\Pi$), *J. Mol. Spectrosc.*, *53*, 150–188.
Moreels, G., and M. Hersé (1977), Photographic evidence of waves around the 85 km level, *Planet. Space Sci.*, *25*, 265–273.
Moreels, G., G. Mégie, A. Vallance-Jones, and R. L. Gattinger (1977), An oxygen-hydrogen model and its application to the OH emission problem, *J. Atmos. Terr. Phys.*, *39*, 551–570.
Nakamura, T., A. Higashikawa, T. Tsuda, and Y. Matsushita (1999), Seasonal variations of gravity wave structures in OH airglow with a CCD imager at Shigaraki, *Earth Planets Space*, *51*, 879–906.
Nakamura, T., T. Fukushima, T. Tsuda, C.-Y. She, B. Williams, D. Krueger, and W. Lyons (2004), Simultaneous observation of dual-site airglow imagers and a sodium temperature-wind lidar, and effects of atmospheric stability on the airglow structure, *Pap. C.2.1-0044-04*, Comm. on Space Res., Paris.
Packer, D. M. (1961), Altitudes of the night airglow radiations, *Ann. Geophys.*, *17*, 67–75.
Pautet, D., and G. Moreels (2002), Ground-based satellite-type images of the upper atmosphere emissive layer, *Appl. Opt.*, *41*, 823–831.
Pautet, D., G. Moreels, P. Rousselot, C. Reylé, J. Clairemidi, and D. C. Boice (2001), Evidence of a 2200 km extended wave system at the mesospause level, *Adv. Space Res.*, *27*, 1195–1200.
Pautet, D., G. Moreels, P. Rousselot, C. Reylé, and J. Clairemidi (2002), Observing at Oukaïmeden through an extended wave system of the upper atmosphere emissive layer, in *Astronomical Site Evaluation in the Visible and Radio Range*, *ASP Conf. Ser.*, vol. 266, pp. 28–35, Astron. Soc. of the Pac., San Francisco, Calif.
Peterson, A. W., and L. M. Kieffaber (1973), Infrared photograhy of OH airglow structures, *Nature*, *242*, 321–322.
Reisin, E. R., and J. Scheer (1996), Characteristics of atmospheric waves in the tidal period range from the zenith observations of the O_2(0,1) Atmospheric and OH(6,2) airglow at lower midlatitudes, *J. Geophys. Res.*, *101*(D16), 21,223–21,232.
Rousselot, P., C. Lidman, J.-G. Cuby, G. Moreels, and G. Monnet (2000), Night-sky spectral atlas of OH emission lines in the near-infrared, *Astron. Astrophys.*, *354*, 1134–1150.
She, C. Y., and R. P. Lowe (1998), Seasonal temperature variations in the mesosphere region at mid-latitude: Comparison of lidar and hydroxyl rotational temperatures using WINDII/UARS OH height profiles, *J. Atmos. Sol. Terr. Phys.*, *60*, 1573–1583.
Shepherd, G. G., et al. (1993), WINDII, the wind imaging interferometer on the Upper Atmosphere Research Satellite, *J. Geophys. Res.*, *98*(D6), 10,725–10,750.
Sivjee, G. G., and R. L. Walterscheid (1994), Six-hour zonally symmetric tidal oscillations of the winter mesopause over the South Pole Station, *Planet. Space Sci.*, *42*, 447–453.
Slipher, V. M. (1929), Emissions in the spectrum of the light of the night-sky, *Publ. Astron. Soc. Pac.*, *41*, 262–263.
Smart, S. W. (1977), *Textbook on Spherical Astronomy*, 6th ed., pp. 58–68, Cambridge Univ. Press, New York.
Stockwell, R. G., and R. P. Lowe (2001), Airglow imaging of gravity waves: 1. Results from a small network of OH nightglow scanning imagers, *J. Geophys. Res.*, *106*(D15), 17,185–17,203.
Störmer, C. (1910), Photographies des aurores boréales et nouvelle méthode pour mesurer leur altitude, *C. R. Hebd. Seances Acad. Sci.*, *150*, 1631–1634.
Störmer, C. (1911), Résultats des mesures photogrammétriques de l'altitude de l'aurore boréale à Bosekop aux mois de février et de mars 1910, *C. R. Hebd. Seances Acad. Sci.*, *152*, 1194–1196.
Swenson, G. R., and C. S. Gardner (1998), Analytical models for the response of the mesospheric OH* and Na layers to atmospheric gravity waves, *J. Geophys. Res.*, *103*, 6271–6294.
Swenson, G. R., and A. Z. Liu (1998), A model for calculating acoustic gravity wave energy flux in the mesosphere from OH airglow, *Geophys. Res. Lett.*, *25*, 477–480.
Swenson, G. R., C. S. Gardner, and M. J. Taylor (1995a), Maximum altitude penetration of atmospheric gravity waves observed during ALOHA-93, *Geophys. Res. Lett.*, *22*(20), 2857–2860.
Swenson, G. R., M. J. Taylor, P. J. Espy, C. S. Gardner, and X. Tao (1995b), ALOHA-93 measurements of intrinsic AGW characteristics using airborne airglow imager and ground based Na wind temperature lidar, *Geophys. Res. Lett.*, *22*, 2841–2844.
Takahashi, H., T. Nakamura, T. Tsuda, R. A. Buriti, and D. Gobbi (2002), First measurement of atmospheric density and pressure by meteor diffusion coefficient and airglow OH temperature in the mesopause region, *Geophys. Res. Lett.*, *29*(8), 1165, doi:10.1029/2001GL014101.
Taylor, M. J., M. B. Bishop, and V. Taylor (1995), All-sky measurements of short-period waves imaged in the OI (557.7 nm) and Na (589.2 nm) and near infrared OH and O_2 (0,1) nightglow emission during the ALOHA-93 campaign, *Geophys. Res. Lett.*, *22*, 2833–2836.
Taylor, M. J., W. R. Pendleton Jr., S. Clark, H. Yakahashi, D. Gobi, and R. A. Goldberg (1997), Images measurements of short period gravity waves at equatorial latitudes, *J. Geophys. Res.*, *102*, 26,283–26,299.
Teitelbaum, H., F. Vial, A. Manson, R. Giraldez, and M. Massebeuf (1989), Nonlinear interaction between the diurnal and semidiurnal tides: Terdiurnal and diurnal secondary waves, *J. Atmos. Terr. Phys.*, *51*, 627–634.
Turnbull, D. N., and R. P. Lowe (1991), Temporal variations in the hydroxyl nightglow observed during ALOHA-90, *Geophys. Res. Lett.*, *18*, 1345–1348.
Vallance-Jones, A., R. L. Gattinger, F. Creutzberg, F. R. Harris, A. G. McNamara, A. W. Yav, E. J. Llewellyn, D. Lummerzheim, M. H. Rees, and I. C. McDade (1991), The Aries auroral modelling campaign: Characterization and modelling of an evening auroral arc observed from a rocket and a ground-based line of meridian scanners, *Planet. Space Sci.*, *39*(12), 1677–1705.
von Savigny, C., et al. (2004), First near-global retrievals of OH rotational temperatures from satellite-based Meinel band emission measurements, *Geophys. Res. Lett.*, *31*, L15111, doi:10.1029/2004GL020410.
Ward, W. E. (1999), A simple model of diurnal variations in the mesospheric oxygen nightglow, *Geophys. Res. Lett.*, *26*(23), 3565–3568.
Zhang, S. P., and G. G. Shepherd (1999), The influence of the diurnal tide on the O(^{1}S) and OH emission rates observed by WINDII on UARS, *Geophys. Res. Lett.*, *26*, 529–532.

J. Clairemidi, F. Dumont, O. Lorin, and G. Moreels, Observatoire de Besançon, F-25010 Besançon, France. (guy.moreels@obs-besancon.fr)
F. Colas, Institut de Mécanique Céleste, Observatoire de Paris, F-75014 Paris, France.
M. Faivre, Astronomy and Physics Department, Clemson University, Clemson, SC 29634, USA.
D. Pautet, Center for Atmospheric and Space Science, Utah State University, Logan, UT 84322, USA.